AIAA JOURNAL
Vol. 46, No. 7, July 2008

Numerical Prediction of Ultraviolet Radiation from Two-Phase Plumes at High Altitudes

Natalia E. Gimelshein,* Robert B. Lyons,† and James G. Reuster†
ERC, Inc., Edwards Air Force Base, California 93524
and
Sergey F. Gimelshein‡
University of Southern California, Los Angeles, California 90089

DOI: 10.2514/1.34762

A multistep continuum-kinetic approach is used to model a steady state plume flow from a Star 27 motor at an altitude of 118 km. Two-way coupled Navier–Stokes equations and the direct simulation Monte Carlo method are used to predict the interaction between plume and atmospheric gases and micron-sized alumina particles from the thruster. A Monte Carlo radiation code that accounts for photon scattering on particles is used to calculate ultraviolet radiation based on the obtained flowfield solutions. Comparison of computed spectral and integral radiant intensity with available flight data is performed. Photon scattering by submicron particles in the 200 to 400 nm range was found to be a dominant process in the far-field ultraviolet emission.

Nomenclature

g = asymmetry parameter
$I_{b\lambda}$ = black body intensity
I_λ = radiative intensity
N = number of emitted rays
n = particle number density
Q_{abs} = absorption efficiency
Q_{sca} = scattering efficiency
r = particle radius
$\mathbf{r}$ = spatial position
T = temperature
κ_λ = absorption coefficient
σ_λ = scattering coefficient
$\boldsymbol{\Omega}_i$ = ray direction

Subscript

i = particle bin number

I. Introduction

Aluminized solid propellant thrusters typically generate micron-sized aluminum oxide particles, with particle phase mass fractions reaching as much as 30% in the plume. The large particle phase mass fractions have a significant impact on the gas flow inside the nozzle (and therefore thruster performance), the near-field plume structure, and the far-field plume–atmosphere interaction structure. The strong influence from alumina particles on the flow structure inside the nozzle and in the plume results in a dramatic effect on radiation signatures, which becomes even more complex when accounting for the process of photon scattering by particles. Significant efforts have been made in the aerospace community toward accurate prediction of aluminum oxide particle impact on thruster performance and exhaust plume structure (see, for example, [1,2]). The majority of the numerical efforts were focused on low-altitude flow regimes in which continuum computational fluid dynamics (CFD) approaches are suitable throughout the flowfield. At high altitudes, the flow nonequilibrium downstream from the nozzle exit is too strong, and the continuum approach becomes unsuitable for predicting plume features. A kinetic approach, such as the direct simulation Monte Carlo method (DSMC), has to be used to obtain credible information on these flows. For sufficiently large thrusters, it is reasonable to use a hybrid approach that applies continuum CFD simulation to the high-intensity nozzle flow and near-field plume and DSMC for the midfield and far-field plume. The major handicap on the development of two-phase capabilities for modeling high altitude plumes is related to the lack of experimental data on particulate and gas properties, as well as multiple uncertainties in the physical models of the interaction of gaseous and particulate phases. The model deficiencies and unknown parameters result in significant numerical underprediction (4 orders of magnitude for the far-field radiation when neglecting scattering [3]) as well as overprediction (up to 2 orders of magnitude in [4]) of total and spectrally resolved radiation emission observed in-flight experiments.

One of the important factors inherent in aluminized propellant plume radiation is photon scattering by alumina particles. Although the contribution of this process for subscale motors (thrust level of 100 N and lower) is expected to be small (see, for example, [5]), for larger motors, the particulate number density is high enough for scattering to be significant. The main goal of this paper is to analyze the effect of photon scattering in large rocket motors at high altitude and compare numerical predictions of total and spectrally resolved radiation in the UV spectrum with available experimental data from the Star 27 motor firing [6].

II. Flow Conditions

Availability of detailed in-flight measurements of UV radiation from second- and third-stage plumes of the Strypi XI rocket provides a solid basis for numerical model testing and validation [7]. These measurements were conducted during the Bow Shock Ultraviolet 2 Experiment flown in early 1991. As part of this experiment, integral and spectrally resolved radiation from the Antares II motor (second stage) and the Star 27 motor (third stage) in the range from 200 to 400 nm were recorded for flight altitudes from approximately 104 to 119 km. For data collection, aft-viewing photometers and spectrometers installed on periscopes were used. Two lines of sight were examined 4 and 25 deg from the rocket centerline.

Presented as Paper 1014 at the 45th AIAA Aerospace Sciences Meeting and Exhibit, Reno, NV, 8–11 January 2007; received 24 September 2007; revision received 26 February 2008; accepted for publication 27 February 2008.

*Consultant.

†Senior Aerospace Engineer, Propulsion Directorate.

‡Research Assistant Professor, Department of Aerospace and Mechanical Engineering.

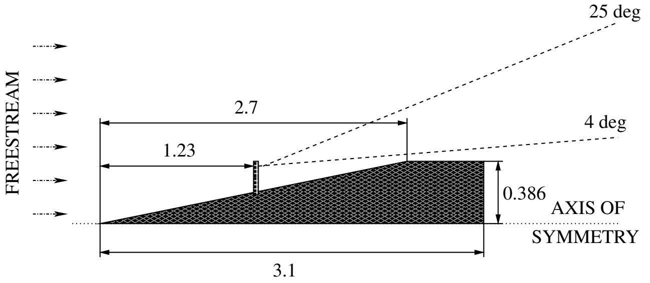

Fig. 1 Schematics of the geometrical setup. All linear dimensions are in meters.

In this work, the point of the flight trajectory that has been numerically examined corresponds to the Star 27 steady state operation at an altitude of 118 km. The geometric setup used to approximate experimental conditions is shown in Fig. 1. The freestream temperature and density are 330 K and 5.21×10^{17} molecule/m^3, and the atmosphere composition is 66.7% N_2, 7.6% O_2, and 25.7% O. The rocket moves with velocity of 2850 m/s; zero angle of attack was assumed in the computations. The nozzle thrust is about 5900 lb. The exhaust gas composition, obtained with a combustion chamber solver incorporated in VIPER code [8] (see next section), is listed as follows: for the species mole fractions, $CO = 0.2225$, $CO_2 = 0.0291$, $Cl = 8.67 \times 10^{-3}$, $H = 0.0190$, $H_2 = 0.2734$, $H_2O = 0.1767$, $HCl = 0.1590$, $OH = 5.38 \times 10^{-4}$, and $N_2 = 0.1108$. The mass fraction of the alumina particles at the nozzle throat is 29.5%, and the assumed particle size distribution there is shown in Table 1. All particles have one of these diameters, and the diameter of a particle does not change in the simulation. The chosen particle distribution approximates a lognormal distribution, and, although the actual size distribution for a Star 27 motor has not been measured to the authors' knowledge, it is believed to be a reasonable approximation of it. Generally, the alumina size distribution in solid propellant motors is different in the chamber, nozzle, and plume and depends on a number of factors primarily related to breakup and coalescence inside the nozzle, which produces a wide range of particle sizes [9]. The most complete survey of particle size data and related analysis may be found in [10]. The diverging part of the nozzle has an effective 17.2 deg half-angle, expansion ratio of 45.94, and exit plane diameter of 0.486 m.

III. Numerical Approaches

A. General Numerical Strategy

Modeling of a rocket plume expanding into a high altitude atmosphere is a numerically challenging problem primarily due to the large variation in gas density and spatial scales. The flow regime varies from continuum inside the nozzle, to transitional in the near field, to free molecular in the far field of the plume. The scales of interest vary from centimeters inside the nozzle to kilometers in the plume. The change in flow regime makes application of a single numerical approach very difficult. Continuum approaches, such as those based on the solution of Navier–Stokes equations, cannot be applied to describe nonequilibrium flows in the far field of the plume. On the other hand, the use of kinetic approaches, such as DSMC, to predict continuum flow inside the nozzle, although theoretically possible, is prohibitively expensive from a computational standpoint. The factor that simplifies numerical analysis is that the plume flow is typically supersonic, which means that the upstream influence of any specific point in the plume is minimal. Therefore, it is both reasonable and convenient to apply a combined continuum-kinetic technique, with the continuum part of the flow being modeled by a Navier–Stokes solver and the transitional flow computed by a kinetic method. In this work, the following combined multistep technique, schematically illustrated in Fig. 2, has been used.

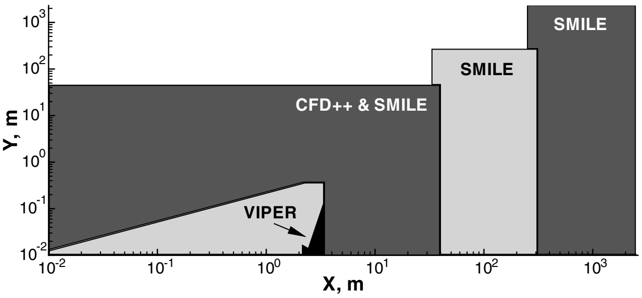

Fig. 2 Schematics of the computational domains used in the present multistep approach.

Step 1: flow inside the nozzle. A continuum method is applied to calculate the flow inside the nozzle. The solution of the parabolized Navier–Stokes equations on a structured grid is obtained with the VIPER code for the two-phase flow inside the diverging portion of the nozzle from the throat to the nozzle exit.

Step 2: plume near field. With the macroparameters at the nozzle exit obtained at step 1 used as the plume inflow boundary conditions, the computation of the plume near field (first 35 m downstream from the nozzle exit) is performed with a density-based Navier–Stokes solver CFD + +. Because the near-field region is the most important part of the flow in terms of particle deflection by plume molecules, the computation has also been performed using a kinetic DSMC-based solver SMILE. The DSMC computation used a starting surface at about 2 m from the nozzle exit plane with the macroparameters at this surface obtained using CFD + +.

Step 3: plume midfield. The CFD + + solution from step 2 is used to obtain macroparameters at a new starting surface at 35 m from the nozzle exit. This surface is perpendicular to the plume axis and expands from the nozzle axis to the radial distance of 20 m. The new surface is used as the plume inflow boundary condition for a DSMC computation of the next 300 m from the nozzle exit. The velocities of molecules entering the computational domain from the starting surface were distributed according to the Maxwellian distribution. Again, the SMILE code was used in the DSMC computations.

Step 4: plume far field. The last step in the flowfield modeling is the far-field computation. The DSMC method is used for this step, and the starting surface obtained from the solution of step 3 is generated at 250 m downstream from the nozzle exit. The ellipsoidal distribution function [11] is used for molecules entering the domain from the starting surface.

Step 5: radiation computation. The UV radiation is calculated using the flow solutions obtained at steps 2–4. A Monte Carlo trajectory-based code, NEMO, developed at the University of Southern California, is used. To compare with experimental data, spectrally resolved and integral radiation was computed along two aft-viewing lines of sight, 4 and 25 deg from the direction of the plume. The detector is located 1.87 m upstream from the nozzle exit plane. Its radial coordinate is estimated to be 0.4 m based off of scaling of [12].

Note that all starting surfaces are located in supersonic flow with the Mach number typically much larger than unity. This guarantees a negligibly small influence of downstream regions on upstream regions, therefore providing smooth step-to-step transitions. Steps 2–4 modeled the interaction of the plume exhaust with the atmosphere. All steps included both gas and particulate phases.

B. Step 1: VIPER Solution Inside the Nozzle

VIPER [8,13] is an axisymmetric parabolized Navier–Stokes (PNS) code that includes finite rate gas chemistry, multiphase capability (via a two-way coupled Lagrangian method), and a variety of mostly empirical models for gas-particulate interaction and particulate evolution phenomena. The PNS scheme is applied from the sonic line near the throat of the nozzle, where particles and gas are assumed to be at equilibrium, to the exit plane of the nozzle. Separate methods are provided to model the combustion chamber and converging section. The combustion chamber pressure and temperature were assumed to be 34.3 atm and 3450 K, respectively. These conditions result in an exit plane gas pressure of approximately 5% of

1 atm, which is expected to be well within the region of applicability of this code.

C. Step 2: CFD + + Modeling of Plume Near Field

The flow solver used to perform the near-field simulation is CFD + + [14,15], developed by Metacomp Technologies, Inc. CFD + + is an unstructured, chemically reacting, multiphase, turbulent, Reynolds averaged Navier–Stokes (RANS) code. It uses a fully implicit, second order in space, second order in time, Harten, Lax, van Leer, contact discontinuity (HLLC) Riemann approximation algorithm, and a modified two-equation κ–ϵ turbulence model. Finite rate chemistry is used for the simulation of the reactions. An Eulerian-based Henderson drag coefficient model [16] is used for the gas-particle flow interactions. A multigrid scheme is used to speed the convergence rate. The simulation assumes that there are precomputed nozzle inflow conditions defined at the exit plane of the nozzle. These exit plane flow conditions are obtained using the VIPER code.

A 2-D axisymmetric grid is used with approximately 50,000 quadrilateral nodes. For simplicity, the nozzle exit plane is assumed to be flush with the base of the vehicle. A sample of the mesh is shown in Fig. 3. Care must be taken such that the initial cell size is significantly resolved to accurately capture the dynamics of the multiphase flow. Too large of an initial grid spacing will lead to improper particle tracking and ultimately an incorrect particle distribution. From a grid resolution study, it was found that an initial grid spacing of 0.001 m was sufficient to preserve accurate particle physics.

Four unique boundary conditions are used for the axisymmetric simulations. The far field has a characteristic-based inflow/outflow boundary condition imposed on it. A symmetry plane boundary condition is imposed at the center line. A Knudsen number-based slip wall boundary condition is used at the body of the missile. Finally, a prescribed inflow condition is used at the exit plane of the nozzle.

D. Steps 3 and 4: SMILE Simulation of Far Field of Plume

The axisymmetric capability of the DSMC-based code SMILE [17] was used as the principal kinetic approach. The important features of SMILE that are relevant to this work are parallel capability, different collision and macroparameter grids with manual and automatic adaptations, and spatial weighting for axisymmetric flows. The majorant frequency scheme [18] was used to calculate intermolecular interactions. The intermolecular potential was assumed to be a variable hard sphere [19]. Energy redistribution between the internal and translational modes was performed in accordance with the Larsen–Borgnakke model. Temperature-dependent relaxation numbers were used. Species weights were used for particulate species. The reflection of molecules on the nozzle and rocket surface was assumed to be diffuse with complete energy and momentum accommodation. The particulate species weights were set to 10^{-9} in step 3 and 10^{-10} in step 4, which implies that the number of real-to-simulated particulates was decreased proportionally. The use of weights allows for a huge reduction in the statistical scatter in particulate properties (the number of simulated particles in parts of the plume with significant particle concentrations was comparable to the number of simulated gas molecules). Very large differences in particle and molecule concentrations minimize the effect of using species weights. The values of particle emissivities, used in SMILE, as well as in VIPER and CFD + +, correspond to the absorption and scattering coefficients used in NEMO (see previous sections). In all codes, the alumina mass density and heat capacity were assumed to be 3970 $\mathrm{kg/m^3}$ and 1775 $\mathrm{J/(kg \cdot K)}$. The alumina crystallization model implemented in SMILE is nonequilibrium according to [20], while CFD + + and VIPER use equilibrium models. To convert from the equilibrium to nonequilibrium model, all particles are assumed to be either fully melted or fully frozen depending on their temperatures.

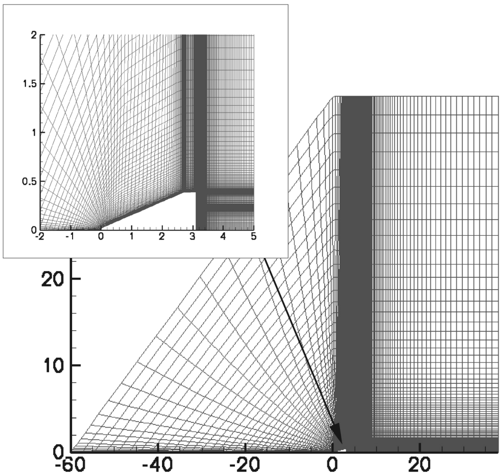

Fig. 3 The mesh used in CFD + + computation of step 2. All dimensions are in meters.

The total number of simulated molecules and particulates in the results presented next was approximately 15 million for step 3 and 10 million for step 4. The number of collision cells for these cases is 4.5 and 3 million, respectively. An automatic adaptation based on the number of particles in cells was used. Note that additional calculations were carried out with 5 and 30 million molecules and 1.5 and 9 million cells for step 3 and 20 million molecules and 6 million cells for step 4, and no visible difference was observed between these and the baseline simulations.

E. Step 5: Radiation Prediction with NEMO

A parallel Monte Carlo radiation code, NEMO, has been developed at the University of Southern California that has 2-D and 3-D modules and generally allows for prediction of radiation from two-phase rocket plumes in the UV, visible, and infrared (IR) ranges. The code's line-by-line capability for the modeling of equilibrium and nonequilibrium radiation from gas media in IR has not been used in this work, and only the description of its UV capability will be given next.

Reverse Monte Carlo Method

For the calculation of radiation intensity from absorbing, emitting and scattering media, the reverse Monte Carlo method [21,22] was used. The reverse Monte Carlo method is based on the principle of reciprocity. The intensity at position $\mathbf{r}_i$ and direction $-\mathbf{\Omega}_i$ is calculated by emitting N rays from point $\mathbf{r}_i$ in the direction $-\mathbf{\Omega}_i$ and tracing them through the medium until they reach a fully absorbing boundary. The path length between scattering events and the direction of scatter are determined from appropriate probability expressions using the local scattering coefficient σ_λ and the phase function. The intensity contributed by each individual path is found by straightening the obtained zig-zag path and performing the standard absorbing-emitting line-of-sight calculation. Because in our case boundaries of the computational domain are nonemitting, the intensity consists only of emission, attenuated by absorption, along the path

$$I_\lambda = \int_0^l \kappa_\lambda(\mathbf{r}')I_{b\lambda}(\mathbf{r}')\exp\left[-\int_0^{l'}\kappa_\lambda(\mathbf{r}'')\,\mathrm{d}l''\right]\mathrm{d}l' \qquad (1)$$

where $l' = 0$ and $l'' = 0$ corresponds to point $\mathbf{r}_i$, κ_λ is local absorption coefficient, and $I_{b\lambda}$ is black body intensity. The total intensity is obtained as average over N such paths.

For scattering, the Henyey–Greenstein approximation was used. The scattering and absorption coefficients and the asymmetry parameter for the particles were calculated as follows. The real part n of the complex refraction coefficient of alumina particles was calculated using the expression given in [23]. The imaginary part was calculated using correlations given in [24]. Then, the absorption and scattering efficiencies $Q_{\mathrm{abs},i}$ and $Q_{\mathrm{sca},i}$, as well as the asymmetry parameter g_i, were calculated using the BHMIE code (originally

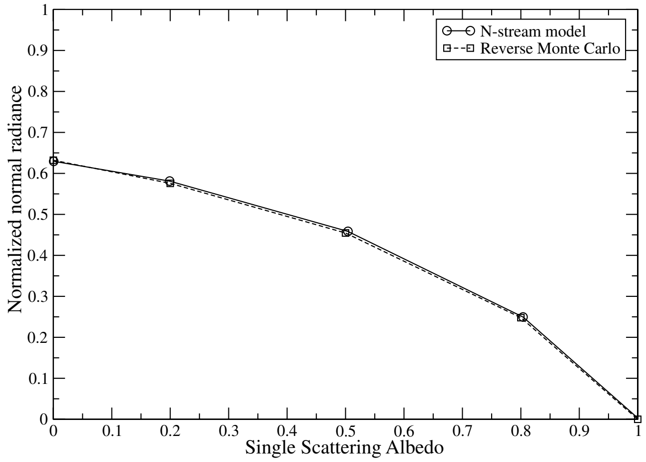

Fig. 4 Normal radiance vs single scattering albedo for a uniform plane parallel medium.

published in [25]) modified by B. T. Draine to include the calculation of asymmetry parameter g) for each particle bin. Scattering and absorption coefficients were calculated by summation over all particle bins

$$\sigma_\lambda = \sum_{i=1}^{N_{\text{bins}}} Q_{\text{sca},i} \pi r_i^2 n_i, \qquad \kappa_\lambda = \sum_{i=1}^{N_{\text{bins}}} Q_{\text{abs},i} \pi r_i^2 n_i \tag{2}$$

where n_i and r_i are the number density and radius of ith particle bin. The asymmetry factor is calculated as follows:

$$g = \frac{1}{\sigma_\lambda} \sum_{i=1}^{N_{\text{bins}}} g_i Q_{\text{sca},i} \pi r_i^2 n_i \tag{3}$$

Because particles in different bins have different temperatures, the product $\kappa_\lambda I_{b\lambda}$ used in Eq. (1) was calculated as

$$\kappa_\lambda I_{b\lambda} = \sum_{i=1}^{N_{\text{bins}}} Q_{\text{abs},i} \pi r_i^2 n_i I_{b\lambda}(T_i) \tag{4}$$

where $I_{b\lambda}(T_i)$ is the black body intensity calculated at a temperature of the ith particle bin.

Radiation Code Validation

To validate the code, reverse Monte Carlo calculations of normal radiance exiting from plane parallel media have been compared with the results obtained by Freeman et al. [26] using a reference discrete ordinate method called N-stream model. The medium optical depth is equal to 1. Because the medium is infinite along the two horizontal directions, specularly reflecting walls are used. The scattering phase function is isotropic. The radiance normalized by the black body intensity is shown in Fig. 4. It clearly shows that there is an excellent agreement between the results obtained with the different approaches.

IV. Modeling of Plume Near Field with DSMC and Continuum Approaches

The primary goal of this work is to estimate the effect of photon scattering from alumina particles on UV radiation in the centerline region and on the periphery of the plume. Accurate modeling of this effect requires reliable prediction of particle distribution in the plume. This is especially important for submicron particles, as they are expected to have the most pronounced impact on scattering due to their very large number densities. The submicron particles essentially follow the gas flow inside the nozzle where the drag force dominates the particle transport. In the plume near field, and in particular in the expansion region near the nozzle lip, the gas density sharply decreases, and the inertia become more and more significant. This creates a difference between the small particle and gas flow velocities at a given position in the flow.

To provide sufficient credibility to the plume near-field solution for gas and particles, two different approaches have been used in this region. First, the Navier–Stokes solver CFD + + was used to compute the region of the flow starting from the nozzle exit plane and expanding 37 m downstream and 40 m in the radial direction. The region in front of the rocket was also simulated to include the possible impact of the freestream on the plume. Second, the DSMC solver SMILE was used in that region with the plume inflow boundary located a few meters downstream from the nozzle exit. This transfer of the DSMC inflow boundary downstream from the nozzle exit plane was necessary because the high gas density in this region makes accurate DSMC modeling in that region extremely expensive from a computational standpoint.

Comparison of gas pressure fields obtained with the kinetic and continuum approaches is presented in Fig. 5. The rocket's leading edge is located at $X = 0$; the black region in the DSMC part of the

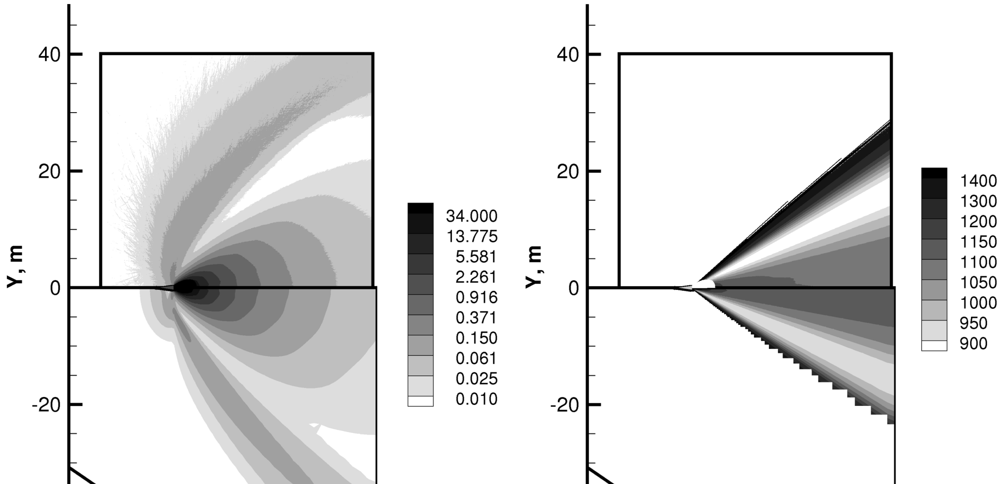

a) b)

Fig. 5 Near-field gas pressure in Pa (left) and particle bin 1 temperature in degree K (right) computed with SMILE (upper parts) and CFD + + (lower parts).

Table 1 Size distribution of alumina particles at the nozzle throat

Bin no.	1	2	3	4	5
Diameter, μm	0.20	3.66	6.11	8.54	11.00
Mass fraction	0.10	0.40	0.30	0.15	0.05

figure illustrates the position of the plume starting surface. There are two regions with elevated pressures: the first (inner) is due to the plume expansion, and the second (outer) corresponds to the interaction region between the hypersonic freestream and the plume. There is a reasonable agreement between the two solutions for the plume region, primarily because the flow is near equilibrium. This is not the case, however, for the plume–freestream interaction region. The freestream mean free path at 118 km is 3 m, which corresponds to a Knudsen number of unity based on the rocket length. This results in the formation of a viscous shock layer characterized by a bimodal molecular velocity distribution. The Navier–Stokes equations are not applicable in this case and are known to significantly underpredict the thickness of the shock front.

The transport of submicron (bin 1, Table 1) alumina particles near the nozzle exit plane is governed by the drag forces from the gas. The agreement between the continuum and kinetic solutions for gas properties in the plume near-field region leads therefore to very good agreement in particle densities. All particles stay in the plume region and do not deflect at angles larger than 40 deg from the nozzle axis. Also, a significant number of particles deflected at an angle of 25 deg, which may lead to scattering from these particles of photons originating in the plume center back to the far-field detector.

Now compare the submicron particle temperatures fields. Comparison of DSMC and Navier–Stokes solutions is presented in Fig. 5. Note first a strong increase of particle temperatures in the radial direction in both solutions. This increase is attributed to the weaker impact of gas cooling for particles moving at larger angles. For a given axial location in the plume, the gas density increases with the decrease in radial distance. Because the gas temperature at any particular point of the plume is lower than the corresponding particle surface temperature, particles are more effectively cooled in the center of the plume than in the periphery. The higher density gas at the plume center allows for more collisions to occur between the gas and the particles thus cooling the particles near the plume center more than those further towards the periphery. Comparison of Navier–Stokes and DSMC solutions shows that the DSMC method predicts about 2% smaller particle temperatures in the core flow (4 deg from the nozzle axis) and over 5% lower temperatures in the periphery (25 deg from the nozzle axis). The main reason for this difference is the gas-to-particles heat transfer models used in the two approaches. A similar difference has been previously observed in [5], in which this difference is analyzed in detail.

Although the uncertainty in particle temperature is not critical for photon scattering by particles, it may have a significant impact on radiation predictions, especially for larger particles that are expected to be the main source of UV radiation. The temperature of these particles in the plume near field was found to be close to the melting point of 2327 K, which in part is related to the liquid-to-solid alumina phase change that occurs in that region. The CFD + + number density fields for these particles are given in Fig. 6. Because of stronger inertia of larger particles, the maximum divergence angle decreases when the particle diameter increases. For 3.66 μm particles (bin 2), the maximum divergence angle is still larger than the far-field photometer angle of 25 deg. However, the number of these particles at 25 deg is three or more orders of magnitude lower than that of the 0.2 μm particles. The contribution of photon scattering and direct emission to the total radiance observed by the far-field photometer will be analyzed next. The maximum deflection angle of the 6 μm and larger particles is much smaller than 0.2 μm particles, and they therefore do not contribute directly to the far-field radiation as measured by the photometer.

The number densities of larger particles obtained by the DSMC method are very similar to the ones obtained by the continuum approach (see Fig. 6) and therefore are not shown here. Quantitative comparison of kinetic and continuum solutions is presented in Fig. 6, in which the number density profiles of 0.2 μm particles are plotted along the radial direction at 16.9 m downstream from the nozzle exit plane. The location $Y = 0$ corresponds to the plume axis. For most of

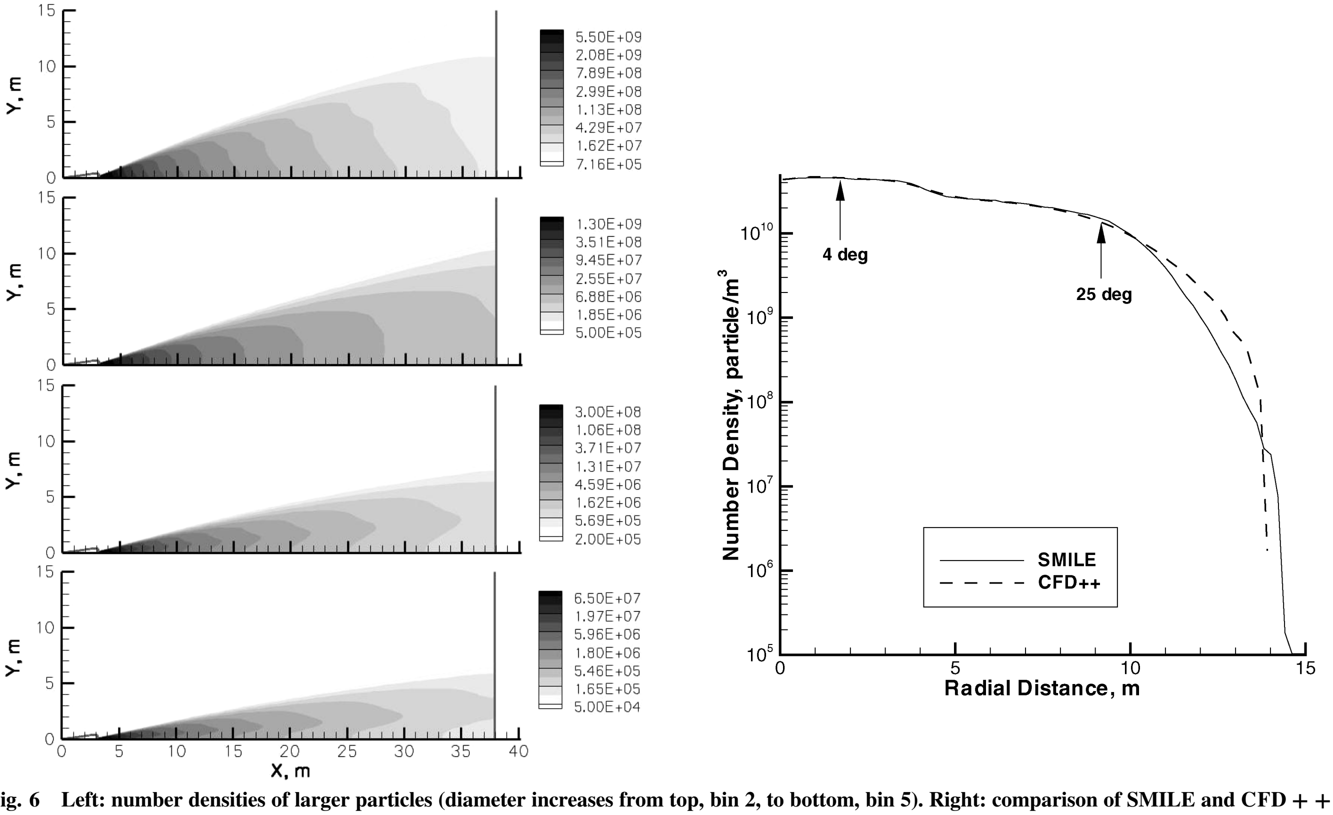

Fig. 6 Left: number densities of larger particles (diameter increases from top, bin 2, to bottom, bin 5). Right: comparison of SMILE and CFD + + particle number densities (bin 1) along a radial cross section at $X = 20$ m.

the flow, especially near the nozzle axis, the solutions agree well within a few percent. There is a noticeable difference for divergence angles larger than 30 deg, in which the particle number density is relatively small. CFD++ assumes small particle number densities to be negligible. During its postprocessing procedure, it clips these small number densities and writes out the value as zero. Therefore, an accurate comparison at these low number densities is not possible.

V. Modeling of Plume Far Field

The near-field computations presented in the previous section were used to generate starting surfaces for successive midfield and then far-field computations. The DSMC method was used in the latter computations. The computational domains used in near and far-field computations are shown in Fig. 7, in which the gas total number densities are plotted. Note that the computational domains overlap. These overlap regions were used to check whether an upstream solution agrees with a downstream one. The good agreement observed between the solutions in the overlap domains serves as the verification of the multistep approach. The higher and lower dashed lines in this figure illustrate 4 and 25 deg lines of sight corresponding to the near-field and far-field photometers.

Initially, the highly underexpanded plume becomes overexpanded at distances larger than 200 meters from the nozzle exit. This overexpansion results in the formation of a weak compression region near the nozzle axis approximately 2 km downstream from the nozzle. The compression region produced due to the freestream–plume interaction, that confines the gas part of the plume, is also clearly visible. The plume–freestream compression region is characterized by elevated gas temperatures, as clearly shown in Fig. 7. The maximum translational temperatures reach over 1000 K in this region, which is unimportant for UV thermal emission.

The number density field of submicron particles is given in Fig. 8. Similar to the previous figure, the dashed lines show the directions of the near-field and far-field photometers. It is clearly shown that there is a large number of small particles present in the field of view of the far-field photometer. For any particular distance from the detector, the particle densities for 25 deg line of sight are within a factor of 2 of the corresponding values for the 4 deg line. It is also important that the particle number density at 25 deg is high enough for photon scattering to be important. Over the first several hundred meters from the nozzle, the 200 nm photon mean free path at 25 deg is less than 10 m, which means that a noticeable number of photons emitted in the core flow near the nozzle axis may be scattered from submicron particles moving in the flow. The number of photons scattered at any given angle, as a function of the scattering angle, is given in Fig. 8. Both the actual phase function calculated with BHMIE and the Henyey–Greenstein approximation used in the present computations are given here for 0.2 μm particles. The key radiation transport process is emission in the core flow followed by scattering by 0.2 μm particles into the 25 deg photometer (in contrast, the 4-deg photometer radiation is dominated by core flow emission). Typical scattering angles for the corresponding photons would be in the range of 150–180 deg. As Fig. 8 shows, there is a significant chance of photon backscattering in this range. Note also the good agreement between BHMIE and its approximation for these angles.

Photon backscattering from larger particles (3.66–11 μm diameter considered in this work) to the far-field photometer is expected to be negligibly small, primarily due to extremely small concentrations of these particles in the side flow. This is illustrated in Fig. 9, in which the number densities of 3.66 μm particles are presented. Although the maximum deflection angle for these particles is larger than 25 deg, their number densities along the 25 deg line are 2 orders of magnitude smaller than the corresponding densities along the 4 deg line, and 4 orders of magnitude smaller than the submicron particle densities. Although the submicron particles are expected to be the main source of photon scattering, they are not a significant source of photon emission. This is primarily due to the relatively low temperatures of these small particles. Because of their size, they are cooled by gas molecules in the plume much faster than

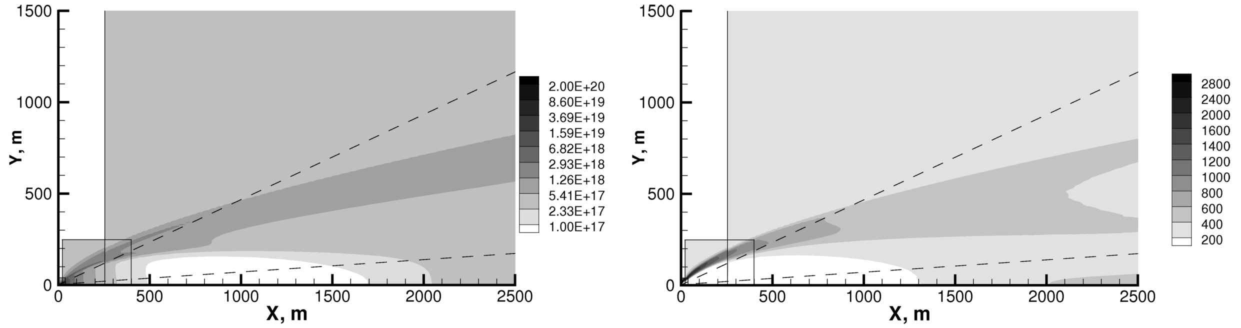

Fig. 7 Gas number density in molecule/m^3 (left) and translational temperature in K (right).

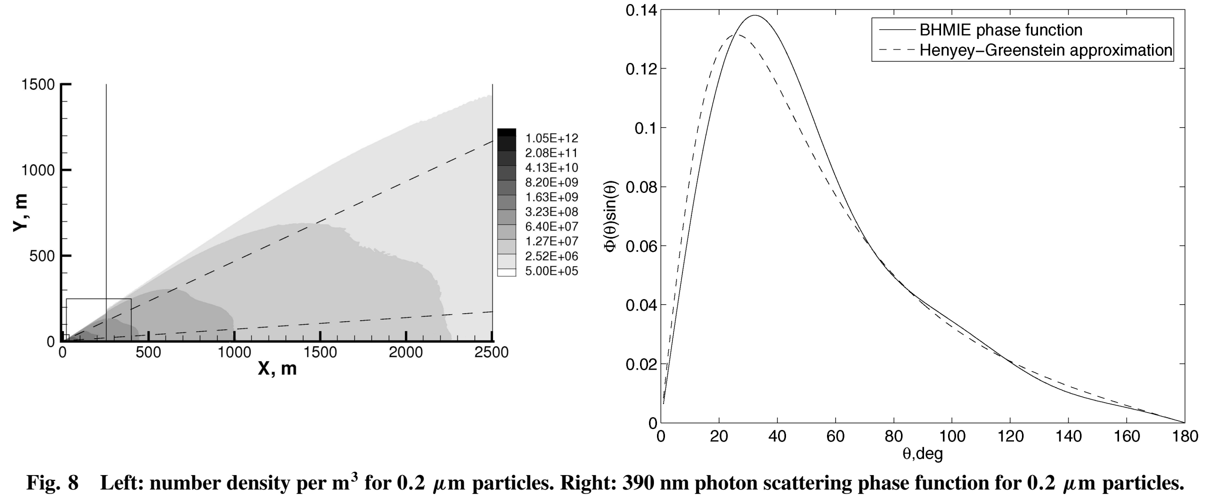

Fig. 8 Left: number density per m^3 for 0.2 μm particles. Right: 390 nm photon scattering phase function for 0.2 μm particles.

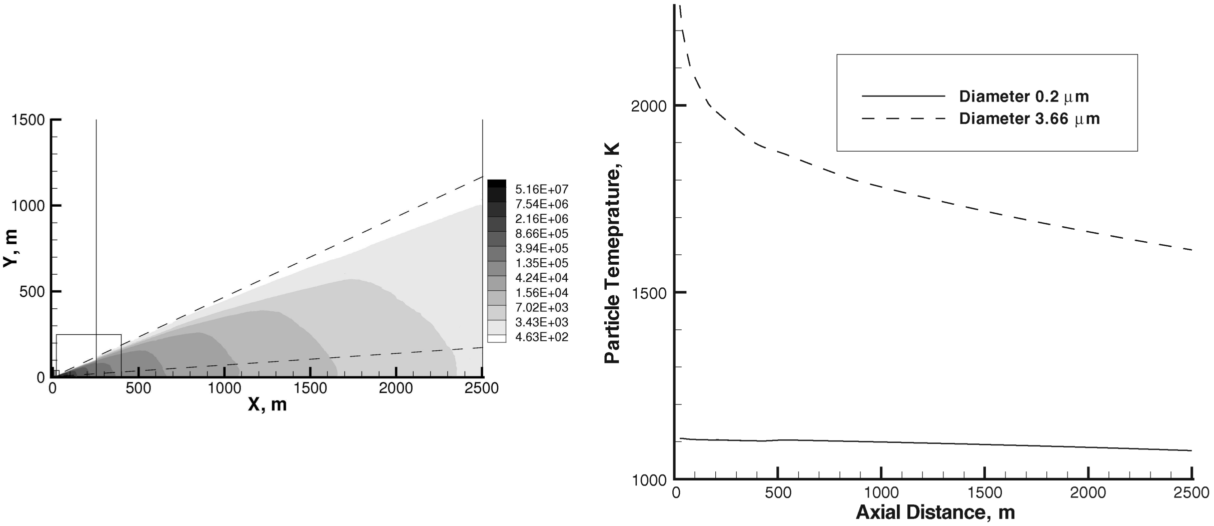

Fig. 9 Left: number density per m^3 for 3.66 μm particles. Right: particle temperatures along the nozzle axis.

the larger particles. Comparison of particle temperatures for the first two particle diameter bins is given in Fig. 9. The large temperature difference at the nozzle exit plane is due to much faster cooling of small particles in the diverging part of the nozzle. The temperature of 0.2 μm particles is slightly over 1100 K at the nozzle exit, and decreases slowly in the plume both due to radiation and gas-particle heat transfer. The temperature of the 3.66 μm particles is much higher in the plume, changing from over 2300 K at the nozzle exit to about 1700 K two kilometers downstream.

Before the comparison of numerical and experimental emission data [6], the sensitivity of computational results to the freestream velocity has been analyzed. During the operation of Star 27 thruster [6], the rocket velocity increased from about 2.5 to over 5 km/s. In the present work, in addition to the baseline 2.85 km/s cases, calculations were conducted for a freestream velocity of 4.6 km/s. The profiles of 0.2 μm particle density and temperature in a cross section located at 2 km from the nozzle exit and perpendicular to the plume axis are given in Fig. 10. Stronger freestream–plume interaction for the elevated velocity 4.6 km/s, that is characterized by larger impact of the freestream on small particles, results in somewhat higher particle temperatures for this case. The impact of freestream of particle density is relatively small, with the particle divergence being a few percent lower. Such an influence is not expected to result in a noticeable change of UV photon scattering from the small particles and was not observed in the 25-deg photometer data.

VI. Ultraviolet Radiation from Star 27 Plume

The particle number density and temperature flowfields obtained by the DSMC method at steps 2, 3, and 4, were combined and interpolated to a nonuniform rectangular grid, which was used to calculate spectral radiance in the range from 200 to 400 nm. To compare numerical results with the experimental data taken by near and far-field photometers [6], the computed radiance values were integrated with a triangular filter over a 51 nm window centered at a wavelength of 230 nm. Let us first analyze the results for the 4 deg line of sight.

Comparison of the calculated UV spectral radiance with the measurements [6] is presented in Fig. 11. Note that no corrective scaling factor of any kind was used for the calculated radiance. The agreement between the calculation and experiment is very reasonable for smaller wavelengths, from 200 to about 300 nm. In this range, the calculated values are about 50% higher then the corresponding measurements. For the wavelengths larger than 300 nm, there is a significant difference between the two. For 400 nm, the calculation overpredicts the experimental data by over an order of magnitude. One of the most probable reasons for such a difference is inadequate values of particle emissivity used in the calculations. Some improvement was obtained in [24] with the use of different particle emissivities. In that work, the computed spectral for larger wavelength was within a factor of 3 of the experimental values. Generally, the expressions for the absorption index used to calculate emissivities as a function of particle size and temperature are not well

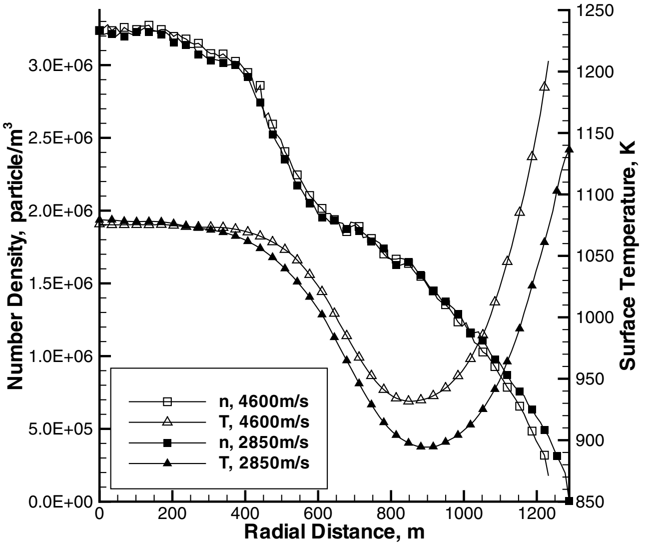

Fig. 10 Number density and surface temperature of 0.2 μm particles for different freestream velocities.

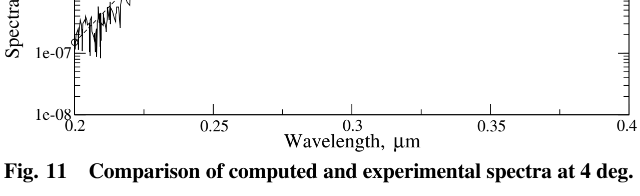

Fig. 11 Comparison of computed and experimental spectra at 4 deg.

known. The uncertainty in emissivity may well approach an order of magnitude [27]. Comparison of expressions of [24] used in this work with values calculated according to experimental recommendations of [28] shows that the experimental values for 1 μm particles at 680 nm are about 6 times lower than those obtained from the expressions in [24]. Obviously, 6 times lower emissivities translate to close to 6 times lower radiance at that wavelength.

The calculated 4-deg line-of-sight radiant intensity integrated over a 51 nm region centered at 230 nm is $4.6 \times 10^{-6} \mathrm{W}/(\mathrm{cm}^2\,\mu\mathrm{m\,sr})$, which agrees reasonably to the measured value of $3.6 \times 10^{-6}\ \mathrm{W}/(\mathrm{cm}^2\,\mu\mathrm{m\,sr})$. Computations have also been performed with photon scattering turned off for all particle bins [the total radiance was $6.21 \times 10^{-6}\ \mathrm{W}/(\mathrm{cm}^2\,\mu\mathrm{m\,sr})$ in this case], and separately for each particle bin with properties taken from the same plume flow predictions. For the latter ones, the results are as follows [$10^{-6}\ \mathrm{W}/(\mathrm{cm}^2\,\mu\mathrm{m\,sr})$]: bin 1, 9.64×10^{-5}; bin 2, 3.16; bin 3, 1.85; bin 4, 1.07; bin 5, 0.39. It is clear that for the 4 deg line, the photon scattering results decrease in radiance. This is related to the shadowing of photons emitted by larger particles by relatively cold submicron particles. As computations for different particle bins show, the main emitters are particles of bin 2 (3.66 μm). The contribution of larger particles is smaller due to their smaller concentrations.

Analysis of the radiant intensity at the 25 deg line from the plume axis shows that the photon scattering process becomes the governing process for larger angles from the plume axis. For the considered 25 deg line, the radiation decreases from $5.71 \times 10^{-9}\ \mathrm{W}/(\mathrm{cm}^2 \cdot \mu\mathrm{m} \cdot \mathrm{sr})$ to $0.021 \times 10^{-9}\ \mathrm{W}/(\mathrm{cm}^2 \cdot \mu\mathrm{m} \cdot \mathrm{sr})$ when the scattering is turned off. The radiance computed for the last four particle bins coincide with that computed without scattering. This shows that all scattering occurs on submicron particles and that the submicron particles' contribution to the photon emission process is negligible. The computed radiation is within a factor of 4 of the measured value in which the calculated radiance was about 5 orders of magnitude lower than the experimental data of $22 \times 10^{-9}\ \mathrm{W}/(\mathrm{cm}^2\,\mu\mathrm{m\,sr})$. Note that no photon scattering was included in [3]. The difference in the current prediction and the data is believed to be primarily due to a significantly larger number of submicron particles in the actual plume compared with the size distribution assumed in this work.

VII. Conclusions

Numerical study of a Star 27 rocket plume at an altitude of 118 km has been conducted. A combined multistep continuum/kinetic approach has been used, with the Navier–Stokes equations being solved inside the nozzle and in the near field, and the DSMC method used in the mid and far fields. All flow solvers used in this work included two-way coupling between the gas flow and alumina particles. Comparison of the continuum and kinetic solutions in the near field showed very good agreement in the plume, both for gas and particulates, and significant differences in the plume–atmosphere interaction region.

The calculated alumina particle properties have been used to calculate spectral radiant intensities in the UV region. The results were compared with available on-board flight measurements for two lines of sight: near field (4 deg from the plume axis) and far field (25 deg). The numerical modeling has indicated that the main process determining the far-field radiation is photon scattering on submicron particles. Accounting for this effect increases the predicted radiance by a factor of 300, and the value of the full radiance at 230 nm in this case is approximately a factor of 4 lower than the measurements. One of the possible reasons for the difference is the uncertainty in the submicron particle size distribution, and thus the results of the work show potential importance of this distribution for accurate prediction of the far-field radiation. The predicted near-field radiation is only about 30% higher than the measurements at 230 nm. This difference increases to approximately an order of magnitude at 400 nm due to inadequate particle emissivity used for this region. The sensitivity of the spectral radiance to particle emissivity, as well as particle size distribution, will be examined in the future work.

Acknowledgments

The work at the University of Southern California was supported in part by the Propulsion Directorate of the Air Force Research Laboratory at Edwards Air Force Base, California. The authors thank Ingrid Wysong for many fruitful discussions.

References

[1] Reed, R. A., and Calia, V. S. "Review of Aluminum Oxide Rocket Exhaust Particles," AIAA Paper 93-2819, 1993.

[2] York, B., Lee, R., Sinha, N., and Dash, S., "Progress in the Simulation of Particulate Interactions in Solid Propellant Rocket Exhausts'," AIAA Paper 2001-3590, 2001.

[3] Candler, G., Levin, D., Branderburg, J., Collins, R., Erdman, P., Zipf, E., and Howlett, C. "Comparison of Theory with Plume Radiance Measurements from the Bow Shock Ultraviolet 2 Rocket Flight," AIAA Paper 92-0125, 1992.

[4] Gimelshein, S. F., Levin, D. A., Drakes, J. A., Karabadzhak, G. F., and Plastinin, Yu. A. "Modeling of Ultraviolet Radiation in Steady and Transient High-Altitude Plume Flows," *Journal of Thermophysics and Heat Transfer*, Vol. 16, No. 1, 2002, pp. 58–67.

[5] Gimelshein, S., Markelov, G., and Muylaert, J. "Numerical Modeling of Low Thrust Solid Propellant Nozzles at High Altitudes," AIAA Paper 2006-3273, 2006.

[6] Erdman, P. W., Zipf, E. C., Espy, P., Howlett, C., Collins, R. J., Cristou, C., Levin, D. A., and Candler, G. V. "In-Situ Measurements of UV and VUV Radiation from a Rocket Plume and Re-Entry Bow-Shock," AIAA Paper 91-0124, 1991.

[7] Smathers, H. W., Horan, D. M., Cardon, J. D., Malaret, E. R., Singh, M., Sorensen, T., Laufer, P. M., Corson, M. R., Brandenburg, J. E., McKay, J. A., and Strunce, R. R. "Ultraviolet Plume Instrument Imaging from the LACE Satellite Strypi Rocket Plume," Naval Research Laboratory, Report NRL/FR/8121-93-9526, Washington, D.C., Sept. 1993.

[8] Kawasaki, A. H., Coats, D. E., and Berker, D. R., "A Two-Phase, Two-Dimensional, Reacting Parabolized Navier–Stokes Sover for the Prediction of Solid Rocket Motor Flowfields," AIAA Paper 92-3600, 1992.

[9] Schmid, O., Reeves, J. M., Wilson, J. C., Wiedinmyer, C., Brock, C. A., Toohey, D. W., Avallone, L. M., Gates, A. M., and Ross, M. N., "Size-Resolved Particle Emission Indices in the Stratospheric Plume of an Athena II Rocket," *Journal of Geophysical Research*, Vol. 108, No. D8, 2003, p. 4250.
doi:10.1029/2002JD002486

[10] Salita, M., "Survey of Recent $\mathrm{Al_2O_3}$ Droplet Size Data in Solid Rocket Chambers, Nozzles, and Plumes," *The 21st JANNAF Exhaust Plume Technology Meeting*, Publication 620, Vol. 1, Chemical Propulsion Information Agency, Columbia, MD, Oct. 1994, pp. 1–17.

[11] Holway, L. H., "Kinetic Theory of Shock Structure Using an Ellipsoidal Distribution Function," *Rarefied Gas Dynamics, Volume 1, Proceedings of the Fourth International Symposium*, edited by J. H. de Leeuw, Academic Press, New York, 1965, pp. 193–215.

[12] Caveny, L. H., and Mann, D. M., "Shock-Layer Induced Ultraviolet Emissions Measured by Rocket Payloads," *Proceedings SPIE*, Vol. 1479, SPIE–International Society for Optical Engineering, Bellingham, WA, 1991, pp. 102–110.

[13] Simmons, F. S., *Rocket Exhaust Plume Phenomenology*, Aerospace Corporation Aerospace Press Series, AIAA, Reston, VA, 2000, p. 286.

[14] Chakravarthy, S., and Peroomian, O., "Some Internal Flow Applications of a Unified-Grid CFD Methodology," AIAA Paper 96-2926, 1996.

[15] Peroomian, O., Chakravarthy, S., and Golberg, U., "A 'Grid Transparent' Methodology for CFD," AIAA Paper 97-0724, 1997.

[16] Henderson, C. A., "Drag Coefficients of Spheres in Continuum and Rarefied Flows," *AIAA Journal*, Vol. 14, No. 6, 1976, pp. 707–708.

[17] Ivanov , M.S., Markelov, G. N., and Gimelshein, S. F. "Statistical Simulation of Reactive Rarefied Flows: Numerical Approach and Applications," AIAA Paper 98-2669, 1998.

[18] Ivanov, M. S., and Rogasinsky, S. V., "Analysis of the Numerical Techniques of the Direct Simulation Monte Carlo Method in the Rarefied Gas Dynamics," *Soviet Journal of Numerical Analysis and Mathematical Modelling*, Vol. 3, No. 6, 1988, pp. 453–465.

[19] Bird, G. A., *Molecular Gas Dynamics and the Direct Simulation of Gas Flows*, Clarendon, Oxford, England, U.K., 1994, p. 458.

[20] Rodionov, A. V., Plastinin, Y. A., Drakes, J. A., Simmons, M. A., and Hiers, R. S., "Modeling of Multiphase Alumina-Loaded Jet Flow Fields," AIAA Paper 98-3462, 1998.

[21] Walters, D. V., and Buckius, R. O., "Rigorous Development for Radiation Heat Transfer in Nonhomogeneous Absorbing, Emitting and

Scattering Media," *International Journal of Heat and Mass Transfer*, Vol. 35, No. 12, 1992, pp. 3323–3333. doi:10.1016/0017-9310(92)90219-I

[22] Modest, M. F., "Backward Monte Carlo Simulations in Radiative Heat Transfer," *Journal of Heat Transfer*, Vol. 125, No. 1, 2003, pp. 57–62.

[23] Dombrovsky, L. A., *Radiation Heat Transfer in Disperse Systems*, Begell House, New York, 1996.

[24] Anfimov, N. A., Karabadjak, G. F., Khmelinin, B. A., Plastinin, Yu. A., and Rodionov, A. V., "Analysis of Mechanisms and Nature of Radiation from Aluminum Oxide in Different Phase States in Solid Rocket Exhaust Plumes," AIAA Paper 93-2818, 1993.

[25] Bohren, C. F., and Huffman, D. R. *Absorption and Scattering of Light by Small Particles*, Wiley, New York, 1982, Appendix A.

[26] Freeman, G. N., Ludwig, C. B., Malkmus, W., and Reed, R., "Development and Validation of Standardized Infrared Radiation Model (SIRRM) Gas/Particle Radiation Transfer Model," USAF/Air Force Rocket Propulsion Lab, Report AFRPL-TR-79-55, Edwards AFB, CA, Oct. 1979.

[27] Duval, R., Soufiani, A., and Taine, J., "Coupled Radiation and Turbulent Multiphase Flow in an Aluminized Solid Propellant Rocket Engine," *Journal of Quantitative Spectroscopy and Radiative Transfer*, Vol. 84, No. 4, 2004, pp. 513–526. doi:10.1016/S0022-4073(03)00268-1

[28] Parry, D. L., and Brewster, M. Q. "Optical Constants and Size of Propellant Combustion Aluminum Oxide Smoke," AIAA Paper 88-3350, 1988.

C. Kaplan
Associate Editor